Composite Structures 313 (2023) 116914

Contents lists available at ScienceDirect

Composite Structures

journal homepage: www.elsevier.com/locate/compstruct

3D printing of continuous carbon fibre reinforced polymer composites with optimised structural topology and fibre orientation

Haoqi Zhang [a], Shuai Wang [b], Ka Zhang [a], Jiang Wu [a], Aonan Li [a], Jie Liu [b], Dongmin Yang [a,*]

[a] School of Engineering, Institute for Materials and Processes, University of Edinburgh, Edinburgh EH9 3FB, UK
[b] State Key Laboratory of advanced Design and Manufacturing for Vehicle Body, College of Mechanical and Automotive Engineering, Hunan University, Changsha 410082, China

ARTICLE INFO

Keywords:
Topology optimisation
3D printing
Fibre orientation
Stress trajectory
Continuous carbon fibre

ABSTRACT

This study presents a sequentially coupled optimisation of structural topology and fibre orientation for 3D printing of continuous carbon fibre reinforced polymer composites. Topology optimisation was first performed to obtain the geometry of the structure under a specific load, and then continuous fibres were placed along the identified principal stress trajectories. Composite preforms were 3D printed by a material extrusion-based technique followed by post-processing with vacuum bagging using epoxy for infusion. The case of Messerschmitt-Bolkow-Blohm (MBB) beam under three-point bending test was studied and a path-based model was also built to analyse the effect of customised fibre placement and their lightweight performance. Experimental results showed that 3D printed composites with optimised fibre orientation achieved 305% and 256% higher strength and stiffness than Markforged® printed composites. By comparing with the traditionally-manufactured composites and aerospace-grade aluminium alloy, this study demonstrated the potential of manufacturing ultra-lightweight composite structures via 3D printing and the benefits of fibre orientation optimisation in lightweight design of composites with topology optimisation.

1. Introduction

Continuous carbon fibre reinforced polymer (CCFRP) composite is an exceedingly high strength and stiffness but low weight composite material [1], which is widely used to meet the requirement of high strength/stiffness-to-weight ratios in aerospace, automotive and infrastructure sectors [2–4]. In some practical situations, where lighter but stiff structures are desired, not every single part of the composites is actually needed. Thus, the removal of these material may remarkably reduce the structure's weight without much negatively changing its stiffness and this can usually be achieved by topology optimisation [5]. Over the past few decades, topology optimisation has been widely used to design structures made of isotropic materials such as steel and thermoplastic, but it is more challenging to implement topology optimisation with the anisotropic materials such as CCFRP composites. According to the research conducted by Lee et al. [6], the topologically optimised structure made of unidirectional (UD) lamina performs badly when Tsai-Wu failure theory is considered. Quasi-isotropic (QI) laminates have also been optimised by using Solid Isotropic Material with Penalization (SIMP) method [7,8] or SIMP-like approaches for the battery-hanging structure [9,10]. However, the challenges of manufacturing were not taken into consideration and the simplification for the manufacturing convenience made the consequence different from the original output to a large extent.

In the traditional manufacturing, the CCFRP structures with topology-optimised geometry have to be machined by mechanical processes such as cutting or drilling, in which the carbon fibres in the structure are cut off, leading to the potential risk of residual defects [11]. In addition, as the fibre direction in the laminates are pre-defined and not confront to the topology-optimised geometry, the reinforcing performances of continuous fibres are not maximised. As an alternative, additive manufacturing (AM) technology has the potential to fabricate composites with highly complex geometries. Among them, the thermoplastic in material extrusion-based 3D printing can be mixed with continuous fibres, and then deposited layer by layer to produce three-dimensional composites [12]. In 2014, Markforged® released the first commercial printer that enabled the 3D printing of composites with 1 K continuous fibre reinforcement [13]. Other researchers also developed in-house printers for CCFRP composites [14,15], which were generally achieved by impregnating the fibres with a thermoplastic matrix prior to

* Corresponding author.
E-mail address: Dongmin.Yang@ed.ac.uk (D. Yang).

https://doi.org/10.1016/j.compstruct.2023.116914
Received 2 July 2022; Received in revised form 6 February 2023; Accepted 8 March 2023
Available online 14 March 2023

extruding or within the printer nozzle. Compared with traditional manufacturing methods, 3D printing of CCFRP offers more design freedom [16] because of the layer by layer deposition of smaller fibre tows (1–2 mm in width). The opportunities arise from 3D printing of CCFRP for controlling fibre arrangement and reducing material waste can be combined with the topology optimisation of composites to achieve lighter and stiffer structures.

Along with the development of 3D printing techniques, new optimisation methods have also been developed for both topology and local material orientation [17,18]. The most popular methods include Continuous Fibre Angle Optimisation (CFAO), Discrete Material optimisation (DMO) [19] and stress-lines method [20]. In the CFAO method, every element in finite element analysis (FEA) equips two variables, *i.e.*, pseudo density which is used to determine the existence of materials, and an angle to determine the local fibre orientation. Jiang et al. used CFAO method to optimise Messerschmitt-Bolkow-Blohm (MBB) beams and performed bending tests [21]. The average stiffness of the sample was increased by 12.4% and 29.9%, compared to the counterparts with horizontal and vertical material orientation, respectively. However, the experimental specimens were manufactured only with the reinforcement of discontinuous fibres. In addition, local optimum usually occurred in CFAO method, which was mainly caused by the transform tensor that contains periodically changing functions. Different from CFAO, DMO method is not likely to encounter the local optima problem. However, the orientation outputs of DMO method were constituted by a set of manually given values, which significantly reduced the design freedom and manufacturing potential as the fibre orientations are highly discretised [22]. As another common approach, the stress-lines method assumes that the highest stiffness would be achieved once fibre paths are in line with the principal stress trajectories. It can be conducted with high computational efficiency without encountering local optima problems. It was proven that the stress-lines method improved the stiffness and led to better stress distributions in the anisotropic materials [12,20]. However, very few experimental tests have been reported to validate this method due to the challenge of controlling continuous fibre paths and the limitations of current 3D printing techniques, in particular the high voids content remaining in the printed parts [23]. The entrapped air voids and physical gaps at layer-layer interfaces result in much lower stiffness and strength than expected [24–26]. Therefore, there is still lack of understanding about the mechanical response and failure process of printed composites with optimised topology and fibre orientation.

In this study, topology optimisation and fibre orientation optimisation were sequentially coupled to achieve better lightweight performance, in which the SIMP method was first performed for the geometry and then the streamlines of principal stress were obtained for the continuous fibre placement. The composite preforms were manufactured with customised fibre placement by the extrusion-based 3D printing technique and then post-processed by vacuum bagging with epoxy powder to achieve a low porosity for experimental validations. The three-point bending tests of MBB beams were conducted to innovatively investigate the mechanical response of composite structures manufactured in accordance with the optimised design, also compared with the benchmark sample that was printed using the commercial Markforged® printing system. In order to further understand the effect of customised fibre paths on lightweight performance, a finite element model based on the actual printing paths was built for the analysis of strain distribution in the topology-optimised geometry and how stress-lines continuous fibres transferred and carried the loading.

2. Sequential coupling of topology optimisation and fibre orientation optimisation

The topology and fibre orientation optimisation method used in this study is sequentially coupled. The first step is the topology optimisation of epoxy, the matrix material of composites, to obtain the geometry. The second step is the fibre placement along principal stress trajectories in the topology-optimised geometry based on the loading condition.

2.1. Topology optimisation

The key objective of topology optimisation in this research is to maximise the global stiffness while removing material that does not contribute much to the stiffness of the composite structure. To represent whether material should exist or not, the whole design domain Ω is first discretised into finite elements, and the pseudo density ρ can be given:

$$\rho(x) = \begin{cases} 0 & if x \in \Omega \backslash \Omega_s \\ 1 & if x \in \Omega_s \end{cases}$$

where Ω_s stands for the area that is constructed by solid material, x stands for a position in the design domain Ω.

Discrete values (between 0 and 1) are then replaced by continuous variables and the SIMP is introduced:

$$E_e(\rho_e) = E_{min} + \rho_e^P (E_0 - E_{min}),\ \rho_e \in [0,1] \tag{2}$$

where ρ_e is the continuous design variable in the interval of $[0,1]$, E_{min} is a very small stiffness of voids which is necessary to prevent singularity of stiffness matrix, and p is the penalisation parameter ($p = 3$ in this case, as widely used in other researches [27–29]). Although the penalisation of density would be more efficient if it takes a relatively high value, the sensitivity will also increase rapidly which makes the optimiser hard to converge [8].

In such a condition, the optimisation problem can be defined as:

$$\min_{\rho}: \quad c(\rho) = U^T K U = \sum_{e=1}^{N} E_e(\rho_e) u_e^T k_0 u_e,\ \rho \in [0,1] \tag{3}$$

$$subject\ \ to: \quad \sum_{e=1}^{N} v_e(\rho_e)/V_0 = f \tag{4}$$

$$KU = F \tag{5}$$

where c is the compliance, U is the global displacement vector, K is the global stiffness matrix,F is the vector of forces applied on the nodes, k_0 is the element stiffness matrix of elements with unit Young's modulus, u_e is the displacement vector of element. v_e is the volume of element, f is the prescribed volume fraction, and N is a set of indices of the elements.

It is worth noting that directly implementing the above steps would possibly result in a structure similar to a checkerboard consisting of alternating solid and void elements, and consequently such structure will be extremely difficult to manufacture. In addition, the optimised structures are usually mesh dependent, which means that once the meshing changes, the outcome structure would become different.

In order to prevent these problems filter techniques were developed, including sensitivity filtering [30], density filtering [31], *etc*. Among them the filter based on a Helmholtz-type PDE developed by Lazarov and Sigmund [32] has been proven to successfully resolve the above issues. It can be described as:

$$-R^2 \nabla^2 \widetilde{\rho} + \widetilde{\rho} = \rho \tag{6}$$

where $\widetilde{\rho}$ denotes the filtered density field and R denotes the radius of the filter. Unlike sensitivity filter and density filter, it does not require information about neighbouring elements but only mesh information, thus more computationally efficient. By using filtered density $\widetilde{\rho}$ instead of ρ, the mesh dependency and checkerboard issues can be avoided.

However, when the value of $\widetilde{\rho}$ is an intermediate value between ρ_{min} and 1, the phenomenon of grey scale would occur, which makes the status of material fuzzy. This is undesirable in topology optimisation especially when manufacturability is considered. In order to address this, Heaviside function developed by Wang et al. [33] is introduced in this research:

$$\overline{\widetilde{\rho}} = \frac{tanh(\beta\eta) + tanh(\beta(\widetilde{\rho} - \eta))}{tanh(\beta\eta) + tanh(\beta(1 - \eta))} \tag{7}$$

where η is the threshold for density, and β is a parameter that controls the slope of the projection process. In this way, filtered density value $\widetilde{\rho}$, which is larger than η, would be projected to 1, and similarly, those smaller than η would be projected to 0, which makes it possible for a result of crisp black and white design with little grey scales.

In order to update material density, sensitivity analysis is proposed:

$$\frac{\partial c}{\partial \rho} = \frac{\partial c}{\partial \bar{\widetilde{\rho}}} \frac{\partial \bar{\widetilde{\rho}}}{\partial \widetilde{\rho}} \frac{\partial \widetilde{\rho}}{\partial \rho} \tag{8}$$

And the method of moving asymptotes (MMA) [34] is utilised to acquire the optimal solution of the problem due to its effectiveness.

The SIMP method for topology optimisation was not only used to capture the geometry of the reference sample, but also applied to the traditionally-manufactured composites and aluminium alloy based on their own material properties (together shown in Table 2), in order to compare their lightweight performance. The geometries after topology optimisation and detailed discussion are presented together with the modelling results in Section 5.3.

2.2. Fibre placement based on principal stress trajectories

Since the mechanical properties of carbon fibres are superior in the fibre direction, continuous carbon fibres should be preferably placed along the direction of maximum tensile and compressive stresses. In other words, the optimised fibre paths align with the stress trajectories which are streamlines based on the orientation of the maximum or minimum principal stress. With the data of in-plane stresses at each node from the finite element analysis, the orientations and values of principal stresses are calculated by Eqs. (9) - (10).

$$\tan\varphi = -\frac{\sigma_x - \sigma_y}{2\tau_{xy}} \pm \sqrt{1 + \left(\frac{\sigma_x - \sigma_y}{2\tau_{xy}}\right)^2} \tag{9}$$

$$\sigma_1/\sigma_2 = \frac{\sigma_x + \sigma_y}{2} \pm \sqrt{\left(\frac{\sigma_x - \sigma_y}{2}\right)^2 + {\tau_{xy}}^2} \tag{10}$$

where σ_x is stress in x-axis direction, σ_y is stress in y-axis direction, τ_{xy} is shearing stress, φ is the angle between the stress normal to the stress trajectories at a point and the x-axis, σ_1 is the value of maximum principal stress, and σ_2 is the value of minimum principal stress. Note that two values of angle φ are calculated for maximum and minimum principal stress.

To demonstrate the above approach for fibre placement, the classical MBB beam with a length of 210 mm and a height of 35 mm (length/height ratio = 6:1) was performed. Only half of the structure with sliding supports was analysed due to symmetry. Fig. 1a shows the dimension of the structure and the position of the external load (a uniform load t in a 2 mm length from the middle top of the beam). The material used in the topology optimisation was epoxy with Young's modulus $E = 3.0GPa$ and Poisson's ratio $\nu = 0.37$. The geometry of the topology-optimised result is shown in Fig. 1b and the fibre placement in the topology-optimised geometry (along maximum and minimum principal stress trajectories) are shown in Fig. 2b, together with other printing paths of 3D printed samples. More details of the printing paths are presented in the following section.

Table 1
Printing parameters for the MBB samples.

	Print temp (°C)	Bed temp (°C)	Printing speed (mm/min)	Nozzle diameter (mm)	Material sources
Markforged	270	room temp	10	1.3	Markforged® cCF & PA-6
cCF/PA-6 preforms	245	room temp	10	1.3	Markforged® cCF

Table 2
The elastic properties of the materials used in the FE modelling.

	Density (g/cm^3)	E_1 (GPa)	E_2 (GPa)	G (GPa)	v12	v21
T300 Carbon Fibre	1.76	230 [41]	–	–	0.2	–
PE6405 Epoxy	1.22	3	–	–	0.37	–
Markforged cCF printed stripe	1.20	54 [42]	7.728	7.625	0.104	0.121
7075 Aluminium alloy	2.81	71.7	–	–	0.33	–
20.6% unidirectional 0° CFRP	1.37	49.762	4.507	1.647	0.335	0.03
20.6% cross-ply CFRP	1.37	27.328	27.328	1.647	0.056	0.056
20.6% quasi-isotropic CFRP	1.37	19.4	19.4	7.295	0.33	0.33
50% unidirectional 0° CFRP	1.54	116.5	8.699	3.188	0.285	0.021
50% cross-ply CFRP	1.54	62.883	62.883	3.188	0.04	0.04
50% quasi-isotropic CFRP	1.54	44.263	44.263	16.716	0.324	0.324

3. Manufacturing and testing

In this section, the manufacturing process of the 3D-printed samples and the experimental test setup were presented. The reference sample with optimised fibre paths was prepared via hybrid manufacturing, including the printing of composites preforms and the post-processing with thermosetting epoxy powder. Markforged specimens with continuous fibres were manufactured using the commercial Markforged® printing system (i.e. Mark Two) for the comparison of the state-of-art printing technology.

3.1. Manufacturing

3.1.1. 3D printing of optimised fibre paths

A Prusa i3 MK3s printer was used in this study for the printing of preforms with optimised fibre paths and a Mark Two printer was used for the Markforged sample for comparison. The printing parameters are shown in Table 1. The continuous carbon fibre (cCF) printing filament (with a diameter of 0.375 mm) was sourced from Markforged® and consists of a fibre bundle (approximately 1000 continuous 7 μm diameter carbon fibres) and an impregnated polyamide 6 (PA-6) polymer [35]. Since the cCF filament contains continuous fibres and there was no filament cutter on the Prusa printer, the toolpaths cannot stop and start as they would during thermoplastic printing. Necessary continuous toolpaths (G-code) were generated through a MATLAB script and transferred to the printer. All the samples were printed onto an unheated Garolite print plate which was coated with a layer of PVA, ensuring adequate adhesion during printing.

Detailed printing paths of the MBB samples are shown in Fig. 2. For the Markforged sample, the default material placement method in Markforged® Eiger system was adopted, as shown in Fig. 2a. Two paths of PA-6 and two paths of concentric continuous fibres were printed first as the wall around the geometry singularity and then the CF filaments were printed in a sequence of 0°/+45°/-45°/90° as the primary infill. After that, PA-6 was printed at the interspaces in each layer to fill the remaining gaps. As can be seen, some relatively large resin-rich areas were generated from the Eiger system, even when a placement method with maximum fibre usage was chosen. The volume fraction of carbon fibres was calculated as 17.34% in the printed composite part since a 34.5% fibre volume fraction was declared by Mrakforged® for the cCF filament. For the cCF/PA-6 preforms with optimised fibre paths, the cCF filaments were printed first along the outline of the structure and then

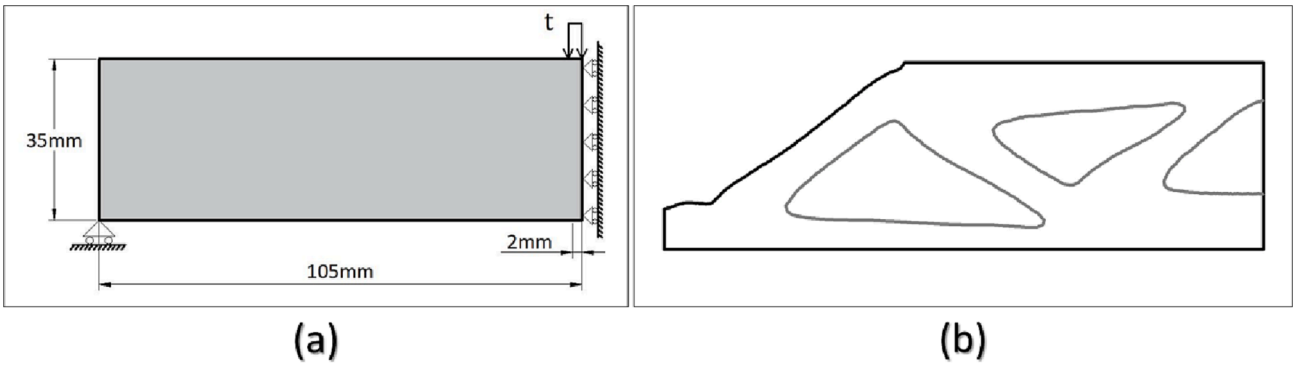

Fig. 1. (a) The domain of MBB beam and (b) the geometry of optimised beam (based on the material properties of epoxy).

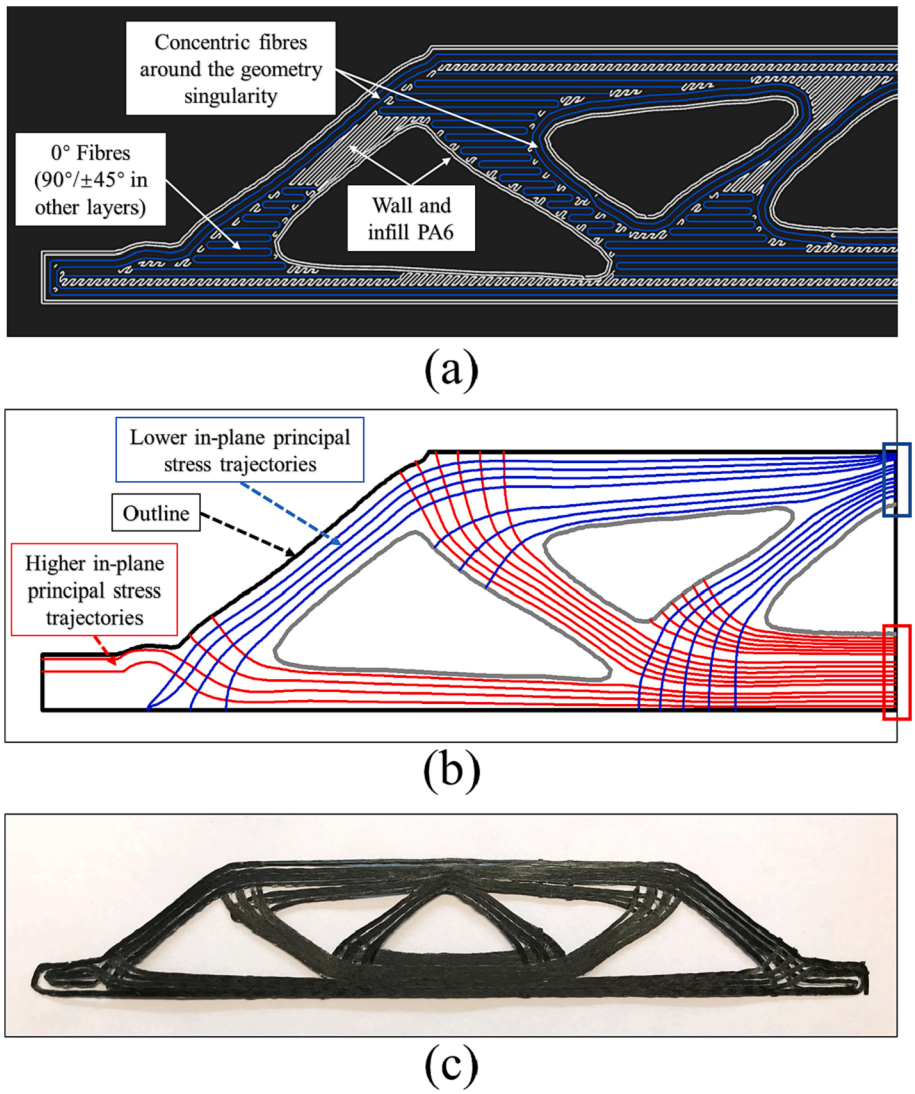

Fig. 2. The printing paths for samples: (a) Markforged and (b) cCF/PA-6 preforms (with optimised fibre paths); (c) the printed single-layer cCF/PA-6 preform.

the maximum and minimum principal stress trajectories in each layer, as shown in Fig. 2b. In this fibre placement method, the coordinates and angles for the maximum/minimum principal stress of each element were imported into Comsol software. The stress trajectories were then generated by entering the start position, gap and number of streamlines in the software, in which we set a consistent distance (0.8 mm, close to the manufacturing limit without critical overlap) of each line at the central part of the domain (shown in Fig. 2b, the red and blue squares) and then the software generated the streamlines to the edge areas based on the orientation of each element. The fibre paths with overlapping with structure outlines were deleted to maintain the originally-designed geometry. An area with denser fibre paths was created in the central area automatically, while a relatively sparse distribution appeared at the edge area. This automatic response of the fibre placement method is to

release the stress concentration around the geometric singularity and enhance the structure, which can also be seen in other research about the stress-lines fibre placement method [36]. In the final step, the end-to-end connection of these streamlines was achieved via Matlab based on the principle of minimising fibre usage and ensuring accurate fibre paths and continuous printing in the domain. A printed single-layer cCF/PA-6 preform was shown in Fig. 2c. Since the rest areas would be infilled by powder epoxy in the post-processing step, the fibre volume fraction of the final composite was calculated as 20.60%. As can be seen in Fig. 2, an excess length of 10 mm was printed on both the left and right ends for all samples so that they can stand on the support properly during the bending test.

3.1.2. Post processing of 3D printed preforms

Considering the gaps between print paths and the weak adhesion between layers, post-processing treatment was needed for the fabrication of a complete three-dimensional sample. The post-processing technique used in this study for cCF/PA-6 preforms was explained in detailed in our previous study [37], in which the thermosetting epoxy powder was sprinkled above and between layers to infiltrate the cCF/PA-6 preforms under vacuum bagging. The curing was first set at 40 °C for 8 h to remove all form of moisture from the powder. The temperature then ramped to 120 °C for 2 h, melting the powder and consolidating the system. Following this, the system was cured at 180 °C for 2 h. The low melt viscosity of epoxy (minimum of 1.26 Pa·s at 120 °C) and the low curing temperature (compared with the melting point of PA-6, 215 °C) enable the composite structures to achieve low porosity whilst still maintaining the curved fibre paths.

3.2. Three-point bending tests of MBB beams

The experimental set-up of the bending test is shown in Fig. 3. The three-point bending tests were performed on an Instron 3360 testing system with a 50 kN load cell, in which the diameter of the loading nose and the support was 5 mm. The span was set to 210 mm and 3D printed fixtures were used to hold the MBB samples. A crosshead speed of 2 mm/min was applied for all tests, while a pre-load 1 mm/min was used to remove slack in the specimen (no data was captured during preload). To measure the 2D strains using digital image correlation (DIC), a fine speckle pattern was applied to the surface of each specimen, as shown in Fig. 5 a & b. All the data obtained from the high-speed and high-resolution camera were processed through an open-source Matlab software called Ncorr [38] to measure the full-field displacement and strain with deviations within 5% for 2D measurement, which was also demonstrated by previous researches [39,40]. To avoid out-of-plane failures such as distortion and instability, all the experimental specimens were manufactured with a thickness of more than 7 mm, *i.e.*, the thickness-to-height ratio is higher than 1:5. Each type of sample consisted of three specimens for the bending test.

4. Finite element modelling

The numerical simulation of the sequentially-coupling optimised sample was built based on the actual printing paths, in order to further investigate the effect of customised fibre paths on stiffness as well as load carrying/transferring. FEM of traditionally-manufactured composites and aerospace-grade aluminium alloy were also performed to compare the lightweight performance and evaluate the engineering potential of the design and manufacturing system in this study.

4.1. Material properties

The material properties used in the modelling are shown in Table 2. The properties of traditionally manufactured composites were obtained based on the rule of mixture (RoM) between T300 Carbon Fibre and PE6405 Epoxy, in which two different fibre volume fractions were performed, 20.6% (the same as the optimised sample) and 50% (approximately the representative high value of the general traditionally manufactured composites) respectively. The lightweight performance will be assessed via the stiffness-to-weight ratio, so only the elastic properties were used in the FE models.

4.2. Modelling based on actual printing paths

As shown in Fig. 4, the finite element model of the sample from sequential coupling optimisation was built based on the actual printing paths. First, the printing paths, i.e. coordinates of the nodes, were imported into Texgen software to obtain the fibre parts of the model (left-hand side in Fig. 4), wherein the 1.0 * 0.1 mm dimension of cross-section was defined by X-ray microtomograph (micro-CT) characterisation in our previous paper [43]. In Texgen software, the fibre parts were meshed with C3D8I solid elements to ensure the accuracy of the simulation and the material direction of each element (fibre longitudinal direction) was defined as the tangent direction of the point on the printing path [44]. The meshed elements were then exported to Abaqus software with an automatically-generated orientation file from Texgen. 70 layers of fibres were embedded into the epoxy matrix in Abaqus to form the final sample (right-hand side in Fig. 4), with the same 7 mm thickness as in the experiment. The left-bottom point of the MBB beam was fixed in order to ensure the convergence of the simulation and the out-of-plane displacement along the thickness direction is unconstrained to test the stability. The two supports were fixed and a displacement was applied to the loading nose along vertical direction. The interaction between the loading nose and the composite beam was defined as 'Hard contact' to only allow normal compression with a penalty in the tangential direction (coefficient of friction = 0.3). The reaction force of

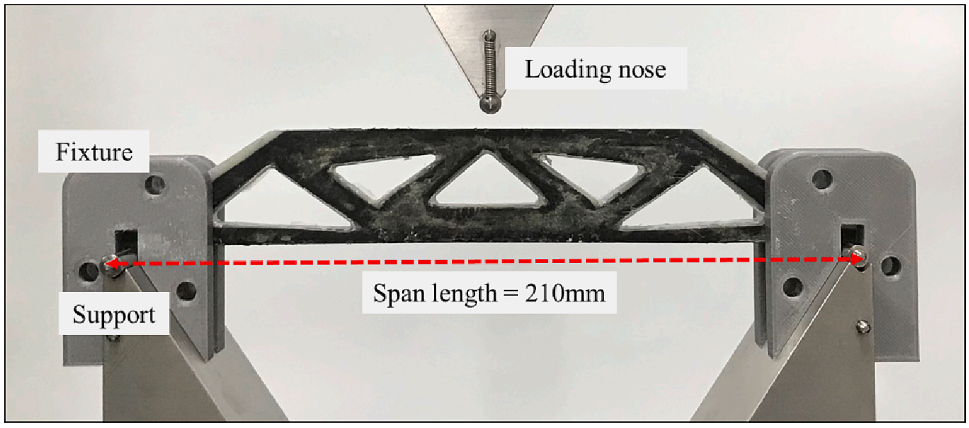

Fig. 3. The set-up of three-point bending test of MBB beam.

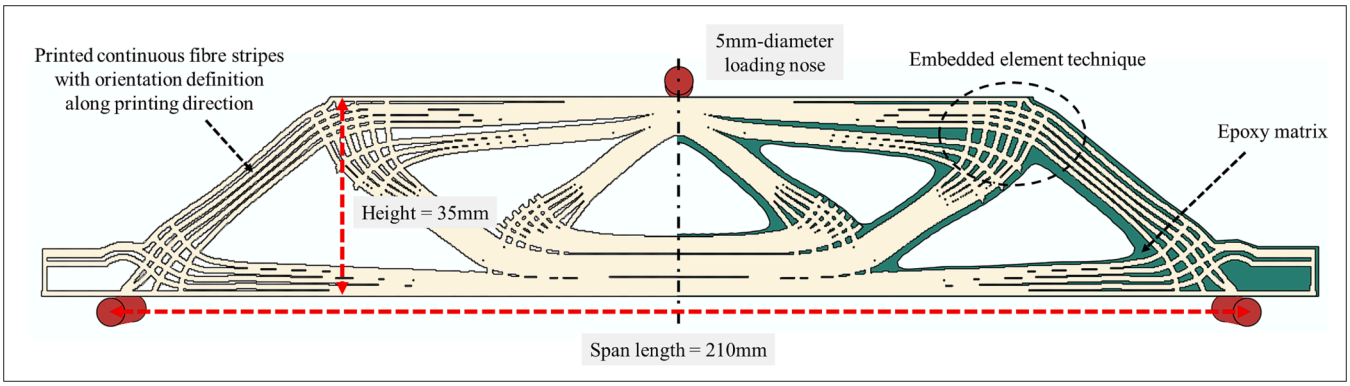

Fig. 4. Path-based model of the sample from sequential coupling optimisation (note that epoxy matrix on the left-hand side was hidden for better visualisation).

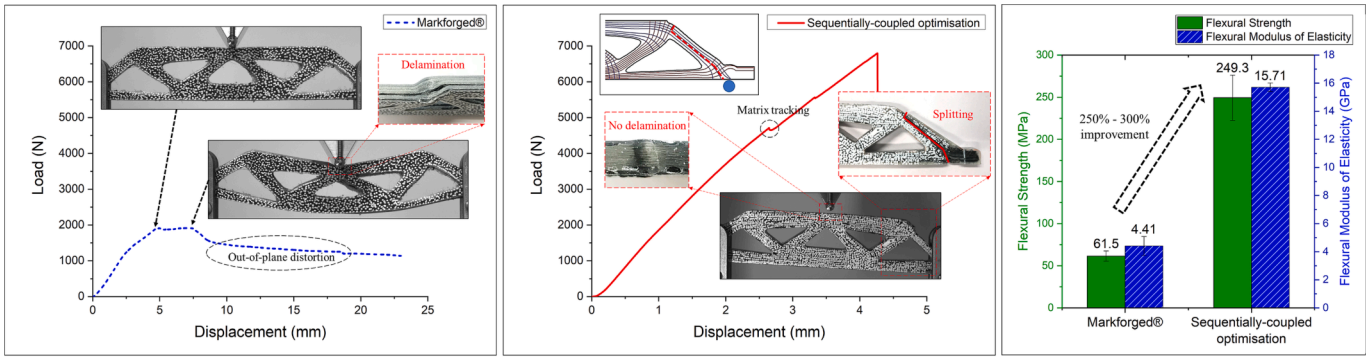

Fig. 5. Load-displacement curves of (a) Markforged and (b) Sequentially-coupled optimisation and (c) flexural strength and modulus of MBB samples.

the loading nose was captured to calculate the stiffness-to-weight ratio. As mentioned, other topology-optimised geometries were simulated with the corresponding material properties shown in Table 2. Same boundary conditions and element types were adopted.

5. Results and discussion

In this section, the experimental results of two printed samples are first presented and discussed, including their mechanical properties and the failure modes in the loading process. Then the mechanism of optimised fibre paths is validated and further discussed via its path-based model. The lightweight performance of the experimental specimens is compared with the modelling results of traditionally-manufactured composites and aluminium alloy.

5.1. Experimental results of 3D-printed MBB beams

The loading processes of 3D-printed MBB beams are shown in Fig. 5. For the Markforged sample, it came to the ultimate load when the delamination happened beneath the loading nose. Then a plateau segment can be seen in the load–displacement curve with the propagation of delamination. After that, the specimen exhibited out-of-plane distortion, leading to a clear drop of carrying capacity. The delamination problem due to the weak layer-to-layer adhesion has also been reported in previous research [13], which was exactly the reason why the post-processing is needed to evaluate the effect of fibre placement method in the test of composites structure.

The response of the specimen with optimised fibre paths is shown in Fig. 5b. Thanks to the reinforcement of optimised placement, no damage was found in the central part of the structure. And no noticeable delamination was seen during the whole loading process, since the post-treatment with powder epoxy sufficiently enhanced the strength between layers. It can be seen that the failure of the specimen began from the location close to the support, in which the matrix cracking happened due to the compression (see the first fluctuation in the curve). However, the fibres along maximum principal stress trajectories here hindered the crack propagation from the matrix and prevented early failure, allowing the further increase of loading. The failure finally happened when the fibres near the support were sheared off at the right-bottom corner. The crack propagated quickly along the right edge of the structure between the adjacent fibres along minimum principal stress trajectories. The failure mode was quite brittle as can be seen from Fig. 5b, along with the splitting of the specimen.

The flexural strength, flexural modulus and stiffness-to-weight ratio were calculated using Eq. (11) – (13):

$$\sigma = \frac{3PL}{2bh^2} \tag{11}$$

$$E_B = \frac{L^3 m}{4bh^3} \tag{12}$$

$$\nu = \frac{E_B}{\rho} \tag{13}$$

where σ is the flexural stress, ε is the flexural strain, E_B is the flexural modulus of elasticity in bending, P is the force, ν is stiffness-to-weight ratio (also called specific stiffness), L is the support span, b is the thickness of samples, h in the height of samples, m is the slope of the tangent to the initial straight-line portion of the load–deflection curve and ρ is the gross density of the structure (disregarding the topology-optimised area). As shown in Fig. 5c, the sample with optimised fibre paths in this study exhibited superior mechanical properties. Compared with the Markforged printed sample, the flexural strength and modulus

were increased by 305% and 256%, respectively. Considering only a small increase of the fibre volume fraction (17.34% vs 20.60%), the superior mechanical properties apparently resulted from the optimisation of the fibre placement as well as the less void content after the post-processing with epoxy infusion.

To further investigate the microstructure of the sample from hybrid manufacturing, SEM characterisation of the cross-sections and fracture profiles are presented. As shown in Fig. 6b, no apparent voids and pores can be seen in the middle-bottom part of the specimen even after the bending test, confirming that the low porosity and good fibre/matrix bonding was achieved via the hybrid manufacturing. However, the localised matrix-rich area in Fig. 6a indicated an uneven fibre distribution for the microstructure of composites, which was mainly due to the original fibre distribution in the Markforged® CF filament [43]. Since the PA-6 matrix had to stay solid during the post-processing to maintain the fibre alignment, the excess PA-6 matrix could not be removed and also a relatively low fibre fraction remained.

5.2. Analysis of optimised fibre paths

Before the discussion of numerical results, the strain distribution and stiffness from experiment were compared to validate the path-based model. Fig. 7 show the strain distribution in the elastic stage between the experimental (captured from DIC) and modelling results. The uniform interval type of distribution was adopted for the legends of all contour plots, in which the contour limit was set as the maximum value of each individual sample to better identify the concentration in the images. As shown in Fig. 7 a & b, the maximum value of Eyy (also the minimum value of Exx) located at the circled area 1 in both numerical and experimental results, which indicated the upper part of the sample was under compression in the longitudinal direction. And the region under the loading nose (area 3, the minimum value of Eyy in both results) was in pure compression. On the contrary, the lower part of the sample (area 2) was under tension in the longitudinal direction. However, the strain distribution of Markforged sample exhibited a different pattern. Because of the lack of continuous fibres and delamination under the nose in area 4 (shown in Fig. 2a and Fig. 5a, respectively), the loading could not be transferred along the longitudinal direction in the upper part. Thus, most of the regions (area 5) were excluded from the load carrying and the loading was concentrated on a small region (area 4) under the loading nose, which dramatically decreased the stiffness of the Markforged sample. The fibre placement issues of topology-optimised geometry and defects of additive manufacturing are exactly the reasons why new design and manufacturing methods in this study are required. The validation of strain distribution also indicated the modelling method based on actual printing paths and embedded element technique can be an effective way to analyse the curved fibre placement in composite structures with complex geometry.

Further, the stress distributions are presented in Fig. 8, in which the embedded fibres are shown to assess their load carrying performance. All the fibres placed along maximum principal stress trajectories were held in the tensile state as designed and with a very even distribution. Similar phenomenon was also found in the fibres along minimum principal stress trajectories. It indicated the stress-lines fibre placement method can be effectively implemented in the complex composite structure after topology optimisation and wherein the superior material properties in fibre direction are sufficiently unitised, especially the high modulus for tension and compression. However, stress concentrations were found in the areas near the supports and loading nose (red circled in Fig. 8). Unlike the structure with homogenised materials, the tailored fibre paths re-distributed the stresses and shifted the stress concentration from the middle part to the area near the supports. Due to the steering of stress-line paths and the inconsistent width in the geometry, the absence of continuous fibres appeared and thus resulted in the matrix damage at corners. Validated with the crack propagation in the experiment in Fig. 5b, the gaps between the adjacent cCF/PA-6 stripes then caused the splitting of specimens at the right edge since they were only filled by epoxy resin. Therefore, it is reasonably assumed that the strength could be further improved and the failure could be postponed if denser continuous fibres were placed in these areas.

5.3. Comparison of lightweight performance

The comparison of lightweight performance is shown in Fig. 9, in which different materials and different fibre fractions of composites were included. It can be seen that the value from FE modelling of the optimised sample is 12% higher than the one from experiment. As mentioned before, this discrepancy was assumed to be caused by manufactured defects including the porosity and fibre misalignment/breakage during printing process [43]. Among the traditionally-manufactured composites, the QI stacking sequence exhibited better performance than the UD and cross-ply composites, with at least 15% higher stiffness-to-weight ratio, since the complex geometries after topology optimisation usually did conform to the 0° or 90° angles and consequently the continuous fibres carried inconsistent loading along the fibre direction. Compared with QI composites, the specimen with

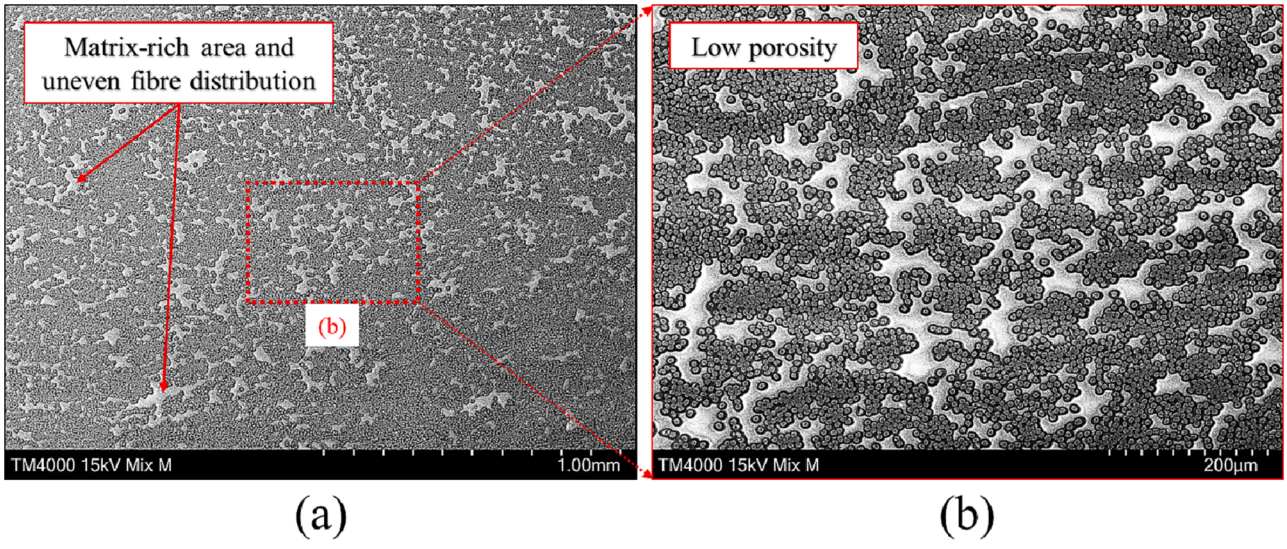

Fig. 6. Cross-section of the middle-bottom part of the 3D printed sample after epoxy infusion.

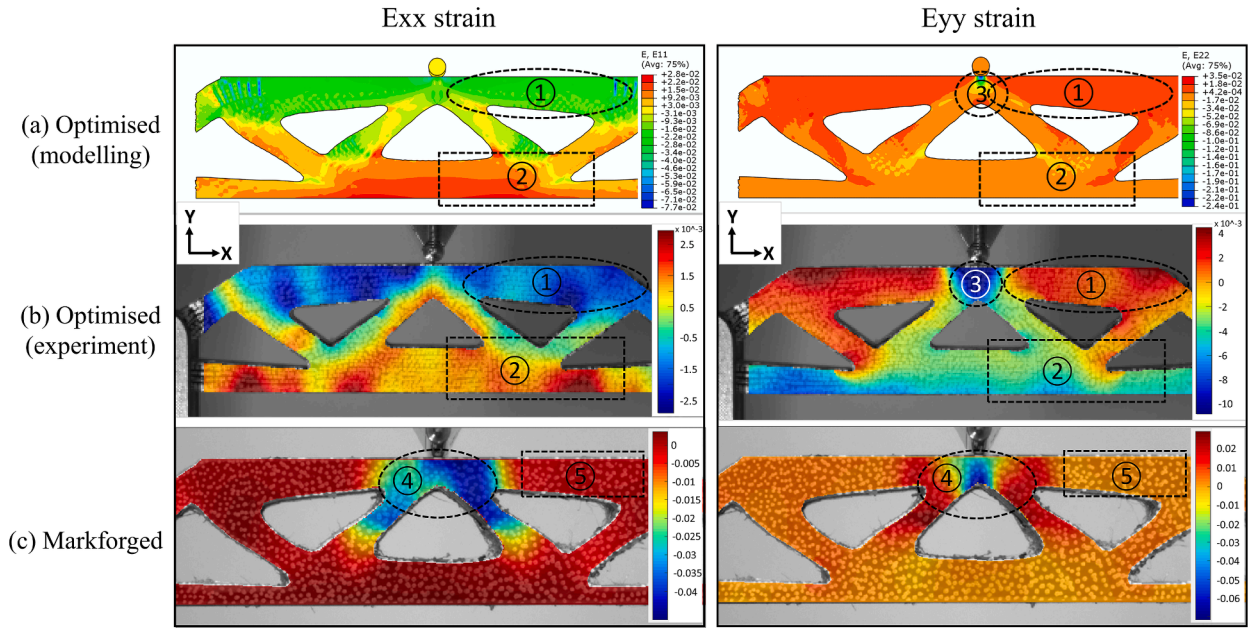

Fig. 7. Strain distributions of sequentially-coupled optimised sample (a) experimental from DIC and (b) numerical from FEM and (c) Strain distributions of Markforged sample.

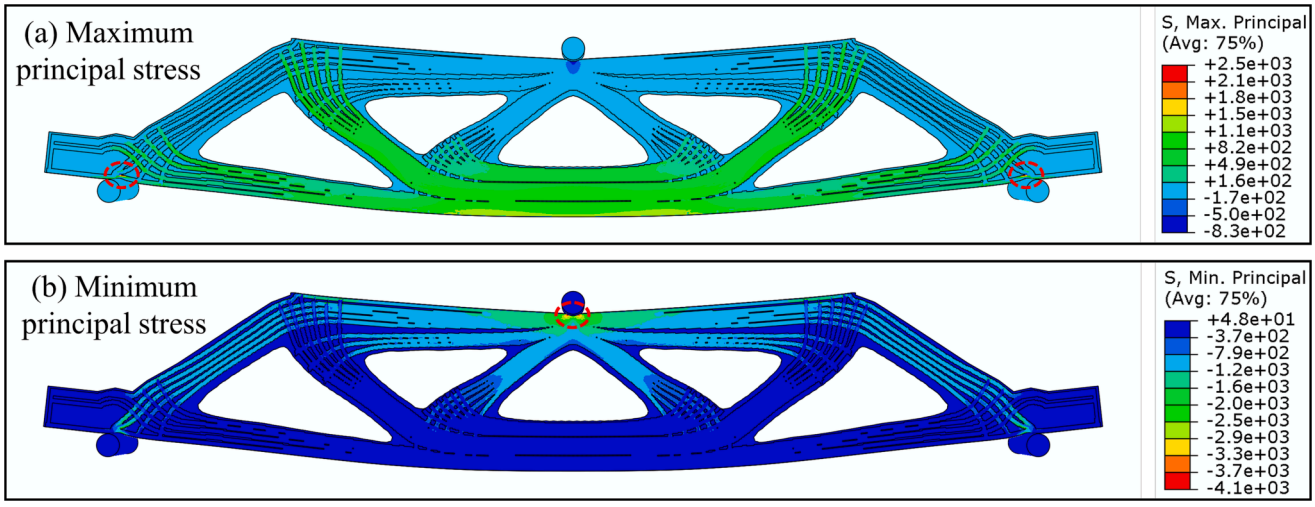

Fig. 8. Distributions of (a) maximum and (b) minimum principal stresses in the sequentially-coupled optimised sample.

optimised fibre paths increased the stiffness-to-weight ratio by about 30% (28% and 37% for fibre fraction 20% and 50%, respectively). For all the composite structures, the lightweight performance would be improved proportionally with the increase of fibre fraction as expected. Beyond that, the aluminium alloy displayed a high stiffness-to-weight ratio among the comparison, and more importantly a competitive lightweight performance as the QI laminated composite (33.5 vs 38.2 $*10^6$ m^2s^{-2}). Only when the fibre placement is tailored according to the loading condition, the continuous carbon fibre reinforced composites exhibit their superior performances (56% higher) against the aluminium alloy under the bending condition in this study.

The distribution of maximum and minimum principal strains in Fig. 10 further explained the improvement brought by optimised fibre paths. The images were captured under 10 mm displacement of the loading nose and the same contour plot legends were applied for different materials (with the highest absolute value in red). For the UD and cross-ply stacking sequences, the concentration of maximum (tension) and minimum (compression) principal strains can be found with a relatively-high value. The distributions in QI composites (same as aluminium alloy) display the dramatically-decreased strains compared with the two former stacking, but the maximum principal strain still concentrated at the mid-bottom part of the structure. Only for the sample with the optimisation of fibre orientation, even strain distributions were achieved (expect for the concentration in the areas close to loading nose and supports), due to the reinforcement of the curved, tailored fibres. The comparison of the deflection can also be seen in Fig. 10. Under the same displacement of the loading nose, the optimised sample exhibited the minimum deflection in the mid-bottom part, which was even better than the UD 0° sample.

6. Conclusions

This paper presented a sequential optimisation strategy for both topology and fibre orientation, in which continuous carbon fibres were placed along the maximum and minimum principal stress trajectories in the topology-optimised MBB structure. Three-point bending tests were

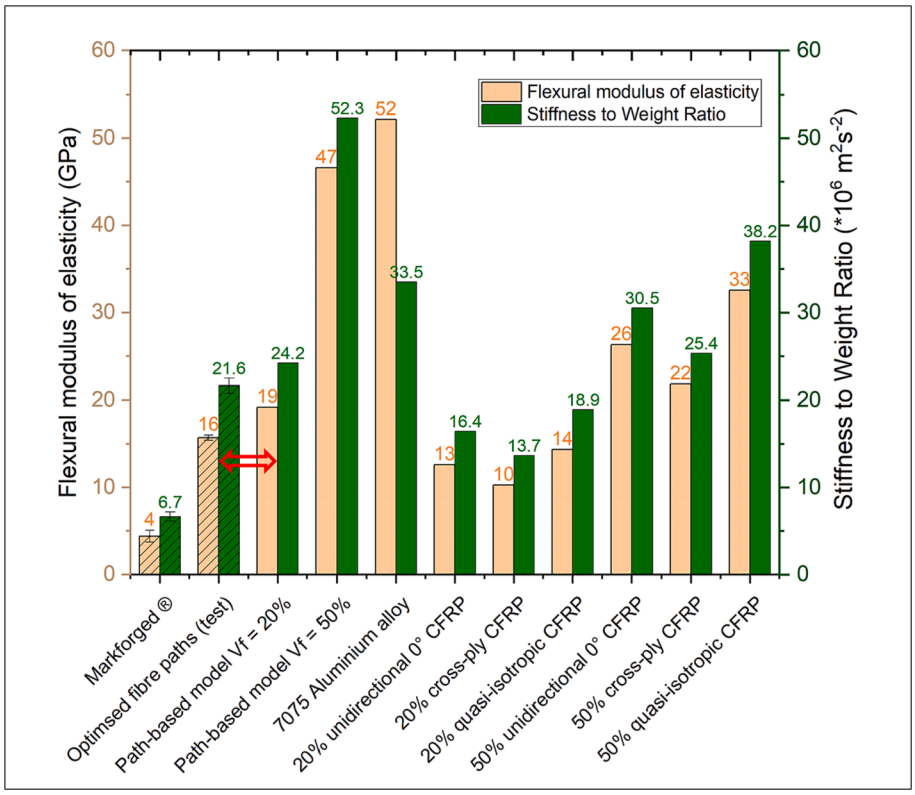

Fig. 9. The comparison of flexural moduli and stiffness-to-weight ratios between different materials.

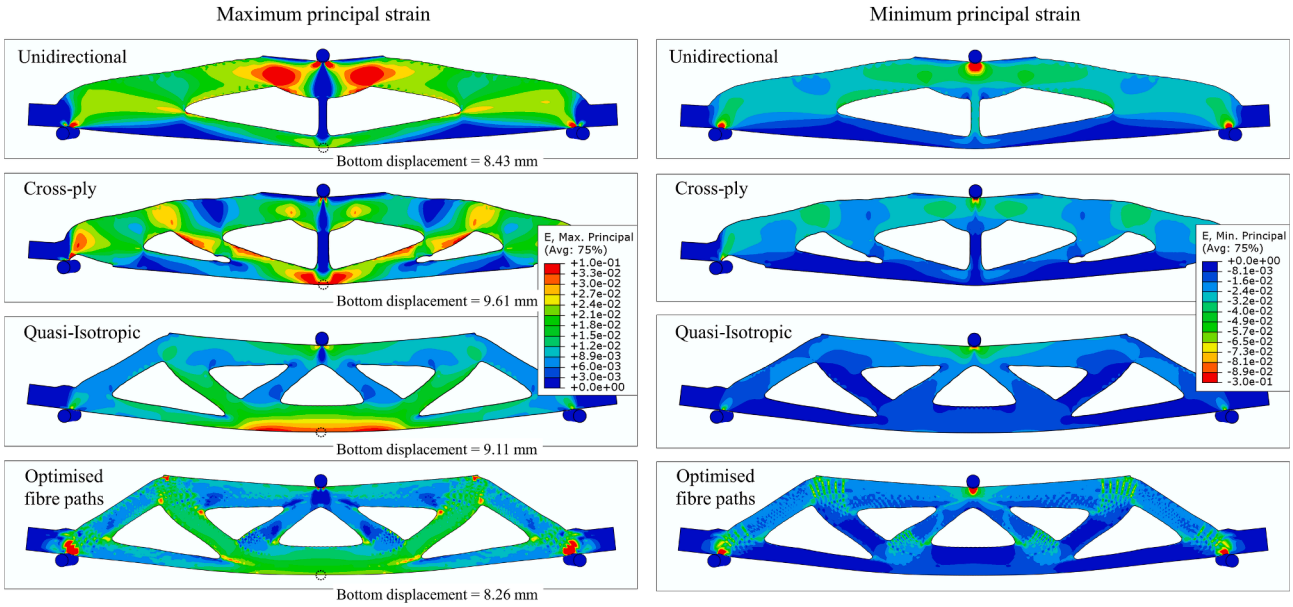

Fig. 10. The distributions of maximum and minimum principal strains among different materials (with loading nose displacement = 10 mm).

conducted to study the mechanical response and compare with Markforged® system. FE models were also built to compare the lightweight performance with that of traditionally-manufactured composites and aerospace-grade aluminium alloy. Main conclusions are drawn as below for the MBB beam under bending that was concerned with in this study:

(1) The Markforged® printing system performed not well enough for manufacturing lightweight composite structures as compared to aerospace-grade aluminium alloys, due to the defects such as weak interlayer adhesion and geometry-based concentric fibre placement.

(2) The optimised sample in this study achieved low porosity and customised fibre paths simultaneously, and thus improved the strength and stiffness by 305% and 256%, respectively. The paths-based modelling also effectively illustrated the benefits of curved fibre placements, in which the optimised fibres were found to be loaded in their fibre direction, in either tension or compression.

(3) As for the comparison with other materials, it was challenging for traditionally-manufactured composites to achieve the lightweight design through the topology optimisation due to the unidirectional fibre

placement within layers, not to mention the manufactured defects from cutting or drilling for complex shapes. Only in combination with fibre orientation optimisation can the composite materials achieve the lightweight design.

Future research is needed to address the overlap issue of fibre paths and to develop the mould-free post-processing technique. More importantly, this study only demonstrated the potential of manufacturing lightweight composite structures via 3D printing. To achieve this, the fibre fraction of the 3D printed composites needs to be substantially increased, for example, by the infill placement of continuous fibres and the fabrication of cCF filament with higher fibre fraction, *e.g.* to 50%.

CRediT authorship contribution statement

Haoqi Zhang: Conceptualization, Methodology, Data curation, Writing – original draft, Visualization, Investigation, Software, Validation, Writing – review & editing. **Shuai Wang:** Data curation, Writing – original draft, Visualization, Investigation, Software, Validation, Writing – review & editing. **Ka Zhang:** Data curation, Writing – original draft, Software, Validation, Writing – review & editing. **Jiang Wu:** Data curation, Writing – original draft, Visualization, Investigation, Software, Validation, Writing – review & editing. **Aonan Li:** Data curation, Writing – original draft, Software, Validation, Writing – review & editing. **Jie Liu:** Supervision, Writing – review & editing. **Dongmin Yang:** Conceptualization, Methodology, Data curation, Writing – original draft, Supervision, Writing – review & editing.

Declaration of Competing Interest

The authors declare that they have no known competing financial interests or personal relationships that could have appeared to influence the work reported in this paper.

Data availability

Data will be made available on request.

Acknowledgement

The authors thank Dr Colin Robert at Edinburgh for valuable discussion on processing of the powder epoxy. DY would like to acknowledge EPSRC CIMComp Hub (EP/P006701/1-RIS3718946) for financial support of a research project linked to this study.

References

[1] Zhang H, Dickson AN, Sheng Y, McGrail T, Dowling DP, Wang C, et al. Failure analysis of 3D printed woven composite plates with holes under tensile and shear loading. Composites Part B: Engineering; 2020. p. 186.
[2] Li N, Link G, Jelonnek J. 3D microwave printing temperature control of continuous carbon fiber reinforced composites. Compos Sci Technol 2020;187.
[3] Parandoush P, Lin D. A review on additive manufacturing of polymer-fiber composites. Compos Struct 2017;182:36–53.
[4] Jenett B, Calisch S, Cellucci D, Cramer N, Gershenfeld N, Swei S, et al. Digital Morphing Wing: Active Wing Shaping Concept Using Composite Lattice-Based Cellular Structures. Soft Robot 2017;4(1):33–48.
[5] Bendsoe MP, Kikuchi N. Generating optimal topologies in structural design using a homogenization method. 1988.
[6] Lee JW, Kim JJ, Yoon GH. Stress constraint topology optimization using layerwise theory for composite laminates. Compos Struct 2019;226:111184.
[7] Bendsøe MP. Optimal shape design as a material distribution problem. Structural optimization 1989;1(4):193–202.
[8] Bendsoe MP, Sigmund O. Topology optimization: theory, methods, and applications. Springer Science & Business Media; 2003.
[9] Dai Y, Feng M, Zhao M. Topology optimization of laminated composite structures with design-dependent loads. Compos Struct 2017;167:251–61.
[10] Chen J, Xu Y, Gao Y. Topology Optimization of Metal and Carbon Fiber Reinforced Plastic (CFRP) Laminated Battery-Hanging Structure. Polymers 2020;12(11):2495.
[11] Davim JP, Reis P. Study of delamination in drilling carbon fiber reinforced plastics (CFRP) using design experiments. Compos Struct 2003;59(4):481–7.
[12] Zhang H, Yang D, Sheng Y. Performance-driven 3D printing of continuous curved carbon fibre reinforced polymer composites: A preliminary numerical study. Compos B Eng 2018;151:256–64.
[13] Kabir SMF, Mathur K, Seyam A-F-M. A critical review on 3D printed continuous fiber-reinforced composites: History, mechanism, materials and properties. Compos Struct 2020:232.
[14] Tian X, Liu T, Yang C, Wang Q, Li D. Interface and performance of 3D printed continuous carbon fiber reinforced PLA composites. Compos A Appl Sci Manuf 2016;88:198–205.
[15] Yamawaki M, Kouno Y. Fabrication and mechanical characterization of continuous carbon fiber-reinforced thermoplastic using a preform by three-dimensional printing and via hot-press molding. Adv Compos Mater 2017;1–11.
[16] Frketic J, Dickens T, Ramakrishnan S. Automated manufacturing and processing of fiber-reinforced polymer (FRP) composites: An additive review of contemporary and modern techniques for advanced materials manufacturing. Addit Manuf 2017;14:69–86.
[17] Gao T, Zhang W, Duysinx P. A bi-value coding parameterization scheme for the discrete optimal orientation design of the composite laminate. Int J Numer Meth Eng 2012;91(1):98–114.
[18] Zhou K, Li X. Topology optimization for minimum compliance under multiple loads based on continuous distribution of members. Struct Multidiscip Optim 2008;37(1):49–56.
[19] Stegmann J, Lund E. Discrete material optimization of general composite shell structures. Int J Numer Meth Eng 2005;62(14):2009–27.
[20] Gea H, Luo J. On the stress-based and strain-based methods for predicting optimal orientation of orthotropic materials. Struct Multidiscip Optim 2004;26(3–4):229–34.
[21] Jiang D, Hoglund R, Smith DE. Continuous fiber angle topology optimization for polymer composite deposition additive manufacturing applications. Fibers 2019;7(2):14.
[22] Nik MA, Fayazbakhsh K, Pasini D, Lessard L. Surrogate-based multi-objective optimization of a composite laminate with curvilinear fibers. Compos Struct 2012;94(8):2306–13.
[23] Blok LG, Longana ML, Yu H, Woods BKS. An investigation into 3D printing of fibre reinforced thermoplastic composites. Addit Manuf 2018;22:176–86.
[24] Pei E, Lanzotti A, Grasso M, Staiano G, Martorelli M. The impact of process parameters on mechanical properties of parts fabricated in PLA with an open-source 3-D printer. Rapid Prototyp J 2015.
[25] Hao W, Liu Y, Zhou H, Chen H, Fang D. Preparation and characterization of 3D printed continuous carbon fiber reinforced thermosetting composites. Polym Test 2018;65:29–34.
[26] Justo J, Távara L, García-Guzmán L, París F. Characterization of 3D printed long fibre reinforced composites. Compos Struct 2017.
[27] Andreassen E, Clausen A, Schevenels M, Lazarov BS, Sigmund O. Efficient topology optimization in MATLAB using 88 lines of code. Struct Multidiscip Optim 2011;43(1):1–16.
[28] Sigmund O. A 99 line topology optimization code written in Matlab. Struct Multidiscip Optim 2001;21(2):120–7.
[29] Rietz A. Sufficiency of a finite exponent in SIMP (power law) methods. Struct Multidiscip Optim 2001;21(2):159–63.
[30] Sigmund O, Petersson J. Numerical instabilities in topology optimization: a survey on procedures dealing with checkerboards, mesh-dependencies and local minima. Structural optimization 1998;16(1):68–75.
[31] Bruns TE, Tortorelli DA. Topology optimization of non-linear elastic structures and compliant mechanisms. Comput Methods Appl Mech Eng 2001;190(26–27):3443–59.
[32] Lazarov BS, Sigmund O. Filters in topology optimization based on Helmholtz-type differential equations. Int J Numer Meth Eng 2011;86(6):765–81.
[33] Wang F, Lazarov BS, Sigmund O. On projection methods, convergence and robust formulations in topology optimization. Struct Multidiscip Optim 2011;43(6):767–84.
[34] Svanberg K. The method of moving asymptotes—a new method for structural optimization. Int J Numer Meth Eng 1987;24(2):359–73.
[35] Chabaud G, Castro M, Denoual C, Le Duigou A. Hygromechanical properties of 3D printed continuous carbon and glass fibre reinforced polyamide composite for outdoor structural applications. Addit Manuf 2019;26:94–105.
[36] Sugiyama K, Matsuzaki R, Malakhov AV, Polilov AN, Ueda M, Todoroki A, et al. 3D printing of optimized composites with variable fiber volume fraction and stiffness using continuous fiber. Compos Sci Technol 2020;186.
[37] Zhang H, Wu J, Robert C, Brádaigh Ó, CM, Yang D.. 3D printing and epoxy-infusion treatment of curved continuous carbon fibre reinforced dual-polymer composites. Compos B Eng 2022:234.
[38] Blaber J, Adair B, Antoniou A. Ncorr: open-source 2D digital image correlation matlab software. Exp Mech 2015;55(6):1105–22.
[39] Ali M, Ab Ghani A, DharMalingam S, Mahmud J. Digital image correlation (DIC) technique in measuring strain using opensource platform Ncorr. Journal of Advanced Research in Applied Mechanics 2016;26(1):10–21.
[40] Kumar SL, Aravind H, Hossiney N. Digital image correlation (DIC) for measuring strain in brick masonry specimen using Ncorr open source 2D MATLAB program. Results in Engineering 2019;4:100061.
[41] INDUSTRIES T. T300-Technical-Data-Sheet. 2018. p. https://www.toraycma.com/wp-content/uploads/T300-Technical-Data-Sheet-1.pdf.pdf (last accessed on 11/04/2022).

[42] Markforged.com. Composites-data-sheet. 2020. p. http://static.markforged.com/downloads/composites-data-sheet.pdf.
[43] Zhang H, Chen J, Yang D. Fibre misalignment and breakage in 3D printing of continuous carbon fibre reinforced thermoplastic composites. Addit Manuf 2021: 38.
[44] Zhang H, Li A, Wu J, Sun B, Wang C, Yang D. Effectiveness of fibre placement in 3D printed open-hole composites under uniaxial tension. Compos Sci Technol 2022; 109269.